Supplementary Information for Self-Powered Perovskite Photodetector with Chocolate-Chip-Cookie Structure

*Ko Ko Shin Thant[1,2], Pimsuda Pangsa-Ngat[1], Patawee Sakata[1,2], Ladda Srathongsian[1,2], Chaowaphat Seriwattanachai[1,2], Myo Zin Tun[1], Phyo Thuta Tun[1,2], Thanawat Kanlayapattamapong[3], Worawut Rueangsawang[1,2], Kanokwan Choodam[1,2], Pipat Ruankham[3], Nattaporn Chattham[4], Ratchadaporn Supruangnet[5], Hideki Nakajima[5], Pongsakorn Kanjanaboos[1,2,6]**

Correspondence: Pongsakorn Kanjanaboos (pongsakorn.kan@mahidol.edu)

[1]Advanced Technologies for Energy and Sustainability Lab, School of Materials Science and Innovation, Faculty of Science, Mahidol University, Nakhon Pathom 73170, Thailand.

[2]Center for Cooling and Energy-saving Materials, Faculty of Science, Mahidol University, Nakhon Pathom 73170, Thailand.

[3]Department of Physics and Materials Science, Faculty of Science, Chiang Mai University, Chiang Mai 50200, Thailand.

[4]Department of Physics, Faculty of Science, Kasetsart University, Bangkok 10900, Thailand.

[5]Synchrotron Light Research Institute (Public Organization), Nakhon Ratchasima 30000, Thailand.

[6]Center of Excellence for Innovation in Chemistry (PERCH-CIC), Ministry of Higher Education, Science, Research and Innovation, Bangkok 10400, Thailand.

MATERIALS AND CHARACTERIZATIONS

Materials: Fluorine-doped tin oxide (FTO) glass substrate (3.2 mm thickness, TEC 15), methylammonium bromide (MABr; 99.99%), and formamidinium iodide (FAI; 99.99%) were purchased from Greatcell Solar. Alconox detergent powder was obtained from Alconox. 15 wt% aqueous colloidal dispersion of tin(IV) oxide nanoparticles was purchased from Alfa Aesar. Cesium bromide (CsBr; 99.9%, trace metals basis), anhydrous N, N-dimethylformamide (DMF; 99.8% v/v), anhydrous dimethyl sulfoxide (DMSO; 99% v/v), Cesium iodide (CsI; 99.9%, trace metals basis), tin(II) chloride dihydrate ($SnCl_2.2H_2O$; 99.999%), anhydrous ethanol (ethanol; 99.5% v/v), acetonitrile (anhydrous; 99.8%), hydrochloric acid (HCl; 37% v/v), 4-tert-butylpyridine (tBP), and lithium bis-(trifluoromethanesulfonyl) imide (Li-TFSI) were all purchased from Sigma Aldrich. Lead (II) bromide ($PbBr_2$; >98.0%) and lead (II) iodide (PbI_2; 99.99%, trace metal basis) were obtained from Tokyo Chemical Industry (TCI). Spiro-OMeTAD (2,20,7,70-tetrakis[N,N-bis(4-methoxyphenyl)amino]-9,90-spirobifluorene) was supplied by Feiming Chemical Limited.

Characterizations: The perovskite films were characterized using a range of structural, optical, and electrical characterization techniques. Surface morphologies and cross-sectional images were examined using an optical microscope and a field-emission scanning electron microscopy (FESEM; JEOL JSM-7610FPlus, tungsten filament, 7 kV, and secondary electron mode). The X-ray diffractometer (Cu anode, detector scan step size = 0.01°, 397.46 s per step, and 2θ = 5° to 50°) was used to carry out different modes of X-ray diffraction (XRD) and grazing incidence X-ray diffraction (GI-XRD) measurements. Ultraviolet photoelectron spectroscopy (UPS) and X-ray photoelectron spectroscopy (XPS) were conducted at beamline 3.2 Ua/b of Synchrotron Light Research Institute (Thailand) using photon energy of 60 eV. The conductive atomic force

microscope (c-AFM) measurements were performed with a Park NX-10 AFM system using a platinum-coated conductive cantilever (ANSCMPC, spring constant $k = 0.036\ N\ m^{-1}$, resonance frequency of 15 kHz), operated at a scan speed of 1 $\mu m\ s^{-1}$ and a contact force of 1 nN under ambient condition (~25°C, ~30% RH). Optical absorption spectra of perovskite films were recorded with a Shimadzu UV-2600 UV–Vis spectrophotometer (slow scan rate, 850–350 nm, and absorbance mode). Steady state photoluminescence spectra were obtained using Horiba FluoroMax4+ spectrofluorometer (1.0 nm increment, 0.5 s integration time, 450 nm excitation source, 10 nm excitation slit, emission wavelength collected between 680 and 850 nm, and 8 nm emission slit). Time-resolved Photoluminescence (TRPL) was measured using Horiba FluoroMax4+ coupled with a Horiba DeltaHub system (excitation: 635 nm NanoLED and detecting emission through a 29.4 nm bandpass with a 675 nm long-pass filter (OD 4.0) from the film side). The kinetic PL intensity trace measurement was conducted using Horiba FluoroMax4+ spectrofluorometer with the continuous excitation of 450 nm at 120 °C while locking down on the emission near 750 nm. External quantum efficiency, responsivity, and specific detectivity were measured using an Enlitech QE-R quantum efficiency system in DC mode with 1 mm^2 beam diameter. For photoresponse testing, devices were illuminated with UVA (365 nm) laser or green (532 nm) laser, modulated by an optical chopper at 1 kHz while the photocurrent was monitored using a Tektronix TBS1072b-EDU oscilloscope.

Electric field and charge generation rate simulations: Finite-difference time-domain (FDTD) simulations (Ansys Lumerical) were conducted for three structural configurations: (i) a 700 nm thick $MAPbI_3$ (MAPI) single layer; (ii) a planar bilayer consisting of a 700 nm MAPI film coated with a 500 nm $CsPbBr_3$ layer; and (iii) a hybrid architecture in which an oblate $CsPbBr_3$ spheroid (lateral radius 1000 nm, height 400 nm, and half-embedded at the film surface) was incorporated

into the upper surface of the 700 nm MAPI film. Refractive index data (n,k) for all materials were sourced from the **refractiveindex.info** database. The simulation domain was set to 2.5 × 2.5 × 2 μm³ with a uniform Cartesian mesh of 5 nm in all directions, which was found to yield mesh-independent results in preliminary simulations. Symmetry and anti-symmetry boundary conditions were applied at the y-min and x-min boundaries, respectively, consistent with x-polarized plane-wave excitation, while perfectly matched layers were imposed on all remaining boundaries to suppress spurious reflections. Each structure was excited by a normally incident periodic plane wave (normalized amplitude and propagating in the z direction) at three discrete wavelengths – 365, 532, and 750 nm chosen to span the UV, visible, and near-bandgap spectral regions of MAPI. Frequency-domain field monitors were used to record the electric field intensity distributions throughout the structures. In addition, the steady-state optical carrier generation rate within the MAPI layer was computed from the simulated power absorption using the CW (continuous wave) generation analysis, enabling quantitative comparison of photogeneration across all three configurations.

Slot-die parameter	Processing window
Gap height	80-100 µm
Coating speed	5 – 10 mm s^{-1}
Dispense rate	0.579 – 1.01 µl s^{-1}
N_2 dried air flow	~10 psi (10 mm height)
Coating temperature	~110 °C

Table. S1 Optimized slot-die processing window parameters for triple cation perovskite.

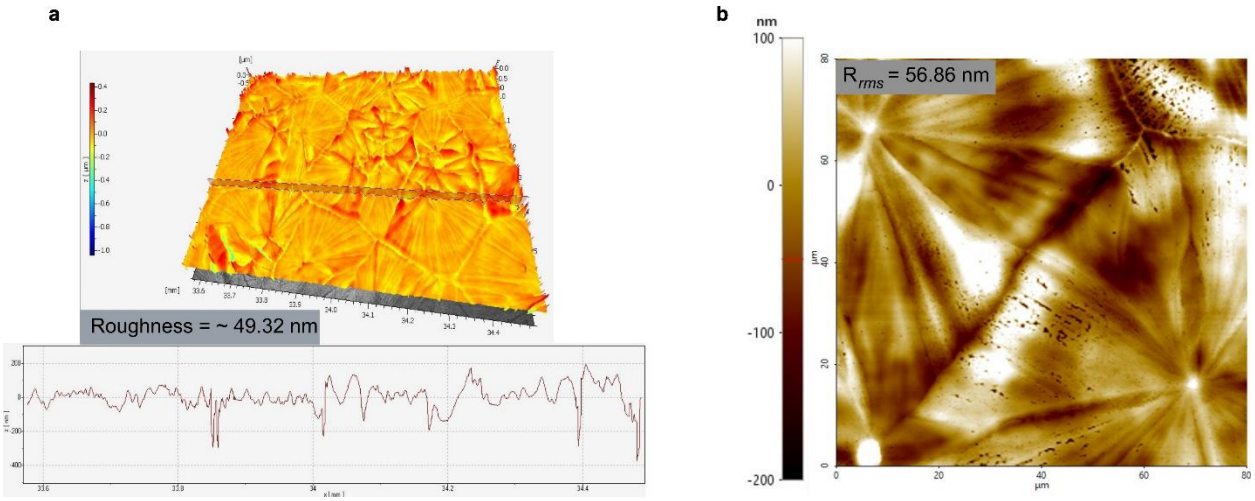

Fig. S1 a 3D profiler and **b** an AFM topography image of slot-die coated triple-cation perovskite.

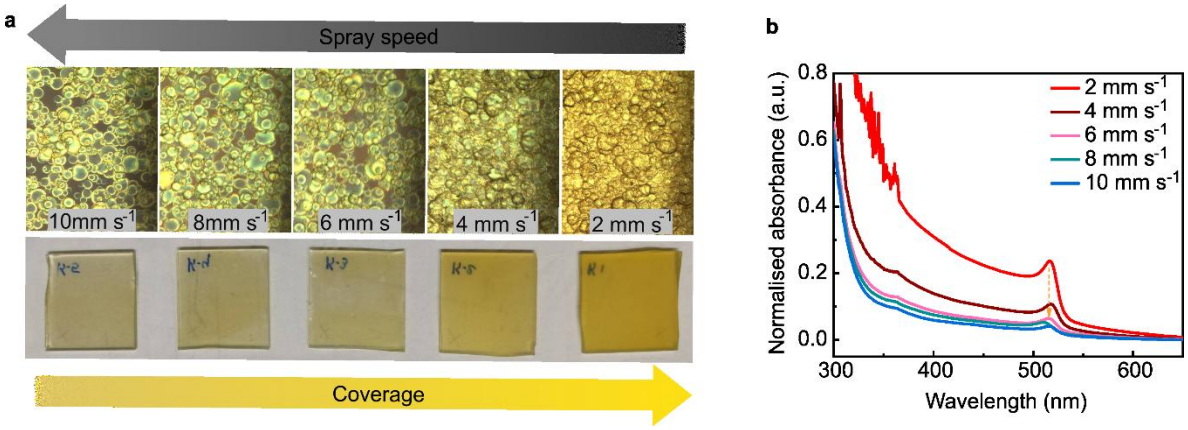

Fig. S2 a Film surface optical images and **b** UV-Vis absorbance spectra of $CsPbBr_3$ with different spray speeds (2 – 10 mm s^{-1}).

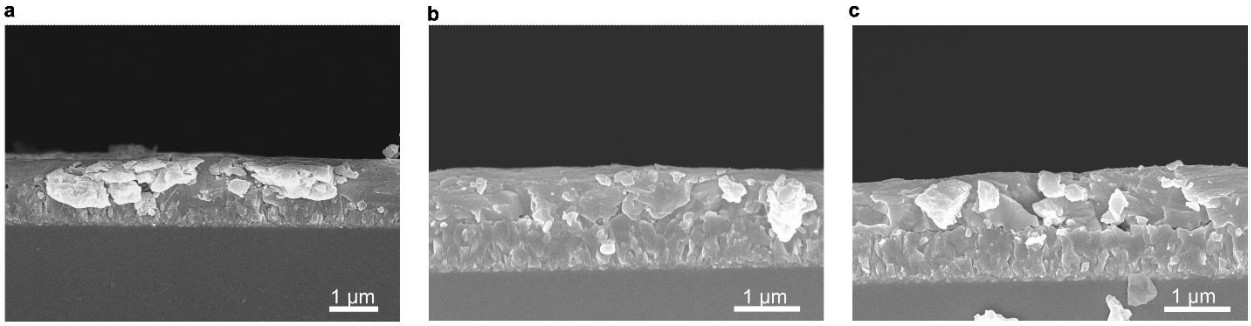

Fig. S3 a-c Cross-section SEM images of hybrid 8 mm s^{-1} perovskite.

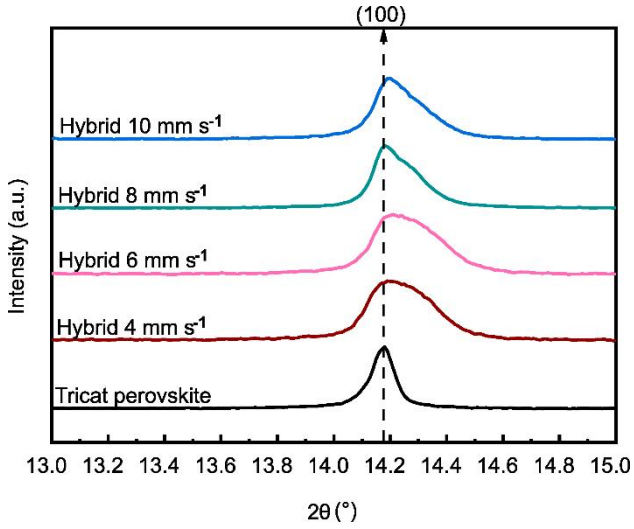

Fig. S4 Zoom-in XRD peaks at (100) plane of control triple-cation and hybrid (4 mm s^{-1} – 10 mm s^{-1}) perovskites.

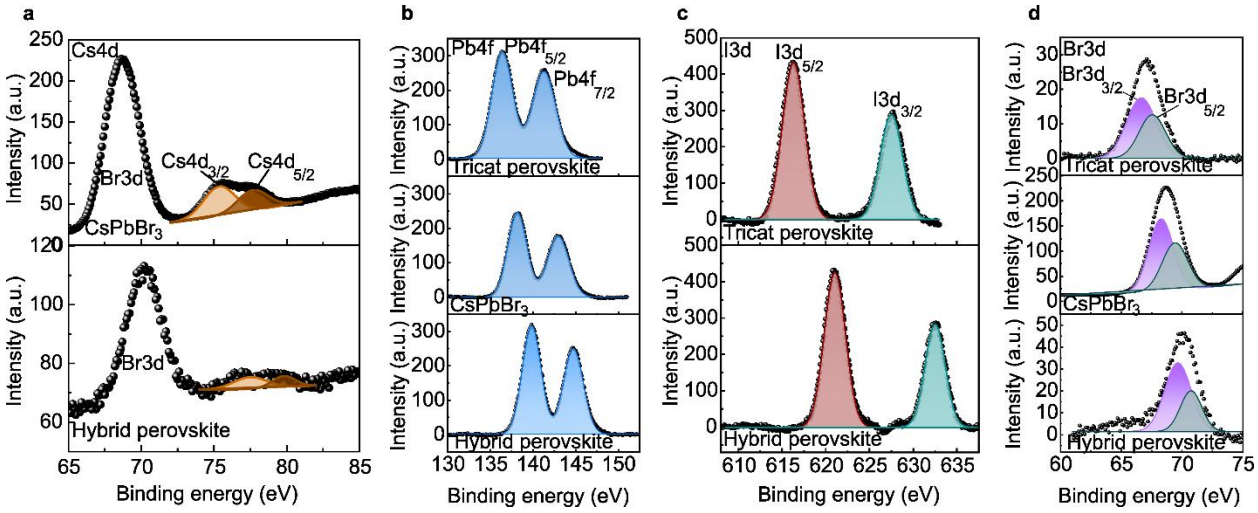

Fig. S5 X-ray photoelectron spectroscopy (XPS) spectra of **a** Cs4d, **b** Pb4f, **c** I3d, and **d** Br3d of triple-cation and $CsPbBr_3$ perovskites.

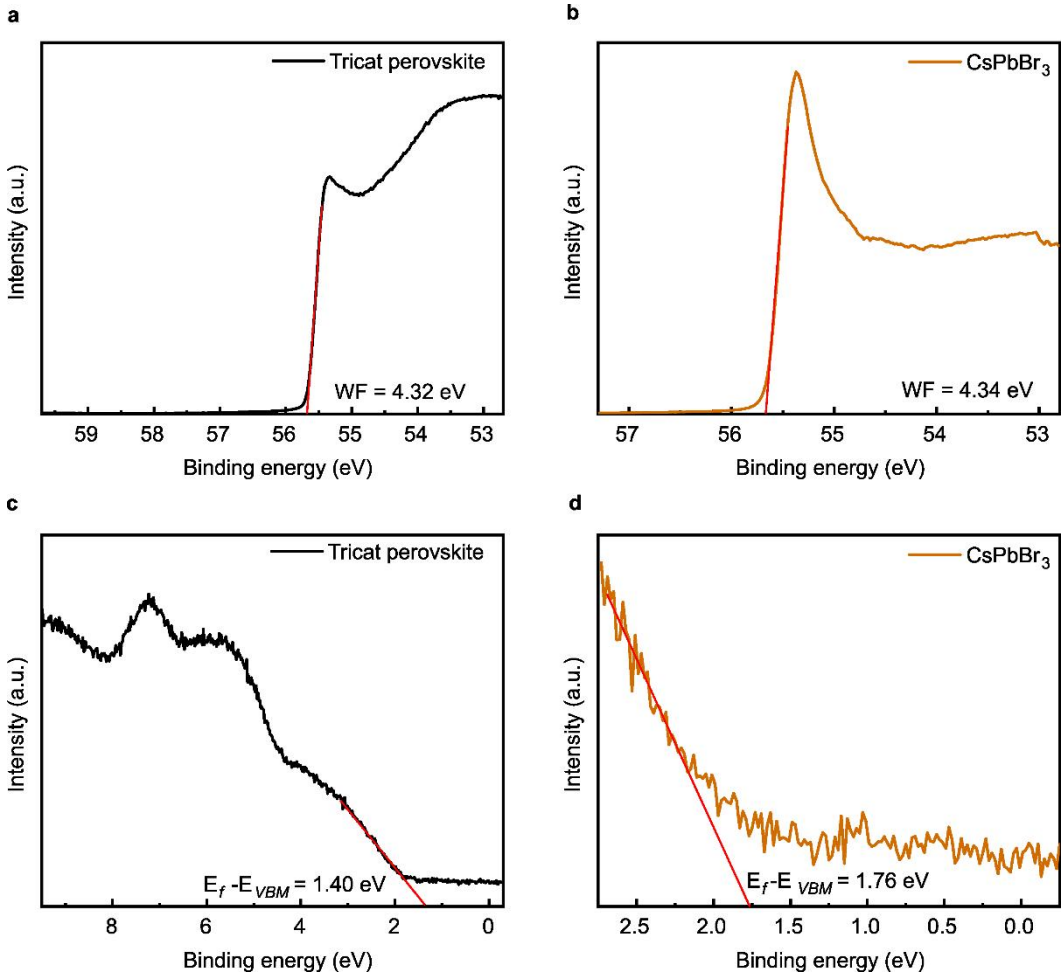

Fig. S6 Ultraviolet photoelectron spectroscopy (UPS) spectra **a, b** at secondary electron cut-off region and **c, d** at the valence band region of triple-cation and $CsPbBr_3$ perovskites.

Perovskite	WF	$E_f - E_{VBM}$	E_g	VBM	CBM
Triple-cation perovskite	4.32 eV	1.40 eV	1.60 eV	-5.72 eV	-4.12 eV
$CsPbBr_3$	4.34 eV	1.76 eV	2.31 eV	-6.10 eV	-3.79 eV

Table. S2 Energy band information from UPS measurement of triple-cation perovskite and $CsPbBr_3$.

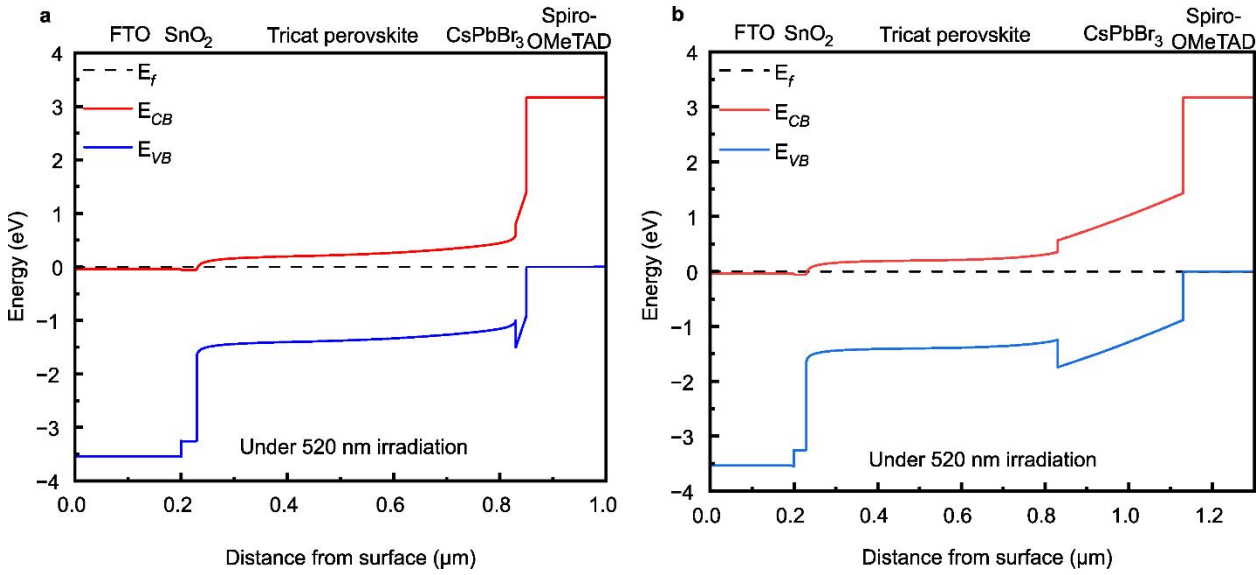

Fig. S7 SCAPS-simulated energy band diagrams of hybrid perovskite devices with $CsPbBr_3$ thicknesses of **a** 20 nm and **b** 300 nm.

Condition	V_{oc} (V)	J_{sc} (mA cm^{-2})	FF	PCE (%)
20 nm	1.16	18.15	25.54	5.46
300 nm	1.35	0.19	12.40	0.14

Table. S3 SCAPS-simulated I-V characteristics of hybrid perovskite devices with $CsPbBr_3$ thicknesses of 20 nm and 300 nm.

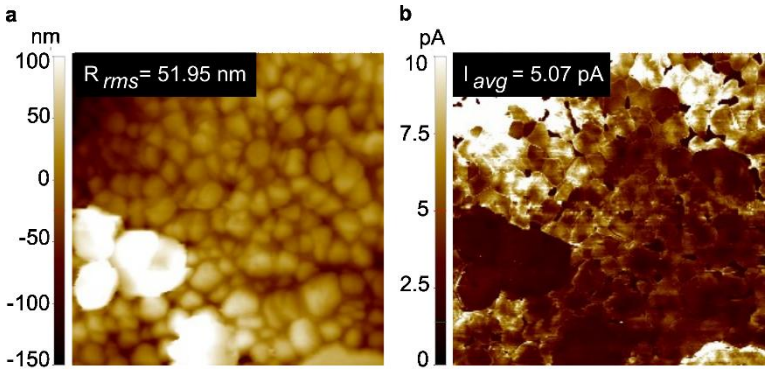

Fig. S8 a Topography and **b** c-AFM current mapping of hybrid perovskite under 656 nm (red laser) wavelength irradiation.

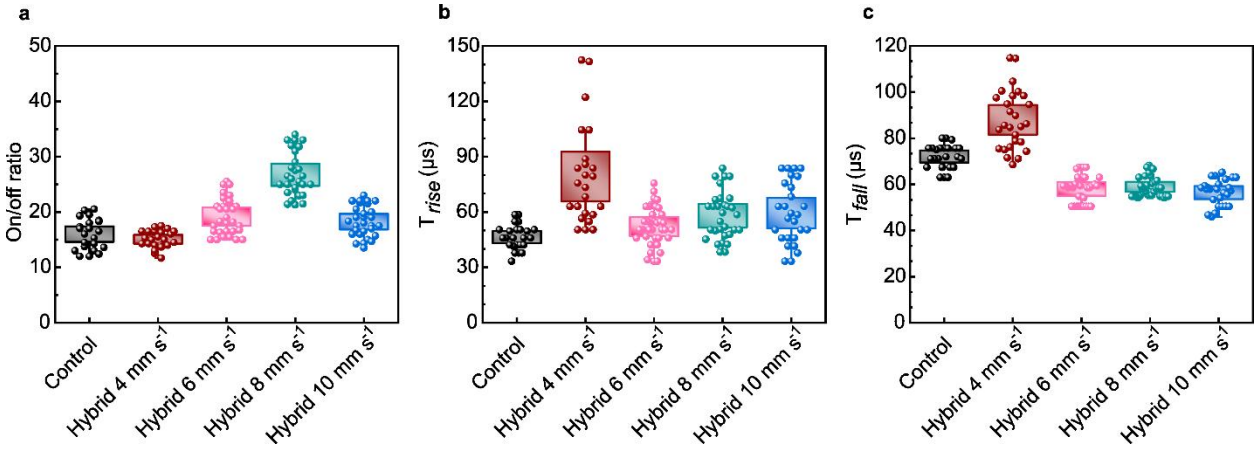

Fig. S9 a-c Statistic photosensor response performance comparison of control triple-cation and hybrid (4 mm s^{-1} – 10 mm s^{-1}) perovskite devices under 532 nm irradiation.

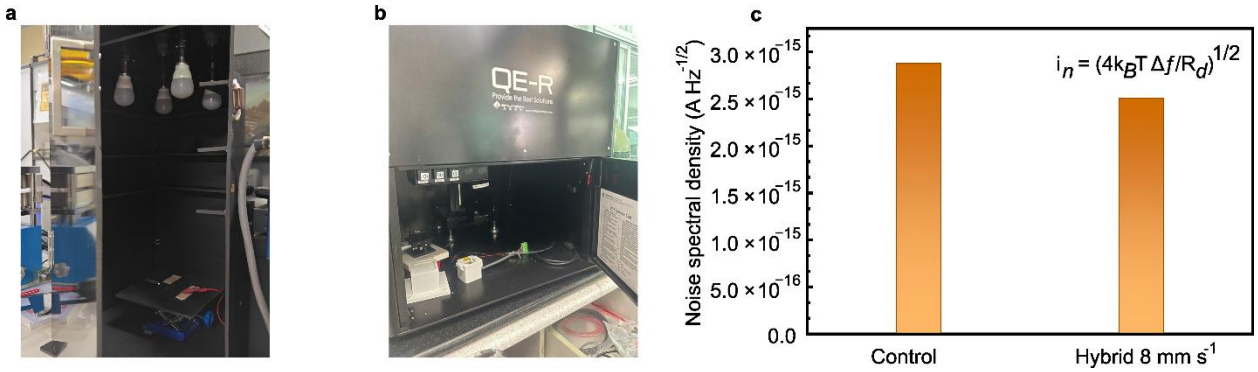

Fig. S10 Photographs of **a** J-V and **b** specific detectivity measurement system. **c** Noise current spectral density of control and hybrid 8mm s^{-1} devices.

Ref	This work	This work	1	2	3	4	5	6	7	8	9

Response wavelength (nm)	**EQE (%)**	**Spectral responsivity (mA W^{-1})**	**Detectivity (cm $Hz^{1/2}$ W^{-1})**	**T_{rise}/T_{fall}**	**On/off ratio**
532	69.39	299.8	5.67×10^{12}	38.3 μs/54.1 μs	34
365	47.38	142.8	2.65×10^{12}	108 μs/120 μs	12
398	15	47	6.87×10^{10}	N/A	N/A
300-400	N/A	4.96	5.4×10^{10}	56 ms/67ms	N/A
395	N/A	359.03	7.95×10^{12}	3.91 ms/4.55ms	N/A
254	25	52.68	4.65×10^{11}	46 ms/47 ms	N/A
254	N/A	49.4	1.2×10^{12}	7.8 μs/33.6 μs	N/A
532	11 @ 5V	50 @ 5V	4×10^{11}	0.4 ms/2.3 ms	2×10^2
546	350 @ -5V	1530 @ -5V	2.17×10^{11}	131 ms/99 ms	10^3
450, 540	-3.7 , 5.7	-13.4 , 24.9	1.1×10^{12}, 2.0×10^{12}	N/A	N/A
405	6400	10100	9.35×10^{13}	N/A	2.1×10^4

Device configuration
FTO/SnO_2(Sol-gel)/SnO_2(Nps)/Triplecation perovskite/$CsPbBr_3$/Spiro-OMeTAD/Au-Ag
FTO/SnO_2(Sol-gel)/SnO_2(Nps)/Triplecation perovskite/$CsPbBr_3$/Spiro-OMeTAD/Au-Ag
ITO/$MAPbCl_3$/PTAA/Al
FTO/Ga_2O_3/$MAPbCl_3$/Spiro-OMeTAD/Ag
ITO/SnO_2/$MAPbCl_3$/PTAA/Au
ITO/$(FAPbI_3)_{0.97}(MAPbBr_3)_{0.03}$/spiro-OMeTAD/Au
$CsPbBr_3$-Cs_4PbBr_6/FTO/TiO_2/
ITO/CsPbBr3/PMMA/Au
ITO/$(BA)_2PbI_4$/Au
FTO/$MAPbBr_{2.2}Cl_{0.8}$/PCBM/PPDIN6/Ag
ITO/TiO_2/$CsPbBr_3$ QDs/Spiro-OMeTAD/Au

Table. S4 Device performance comparison of previously reported perovskite photodetectors with the chocolate-chip-cookie-like hybrid perovskite device (this work).

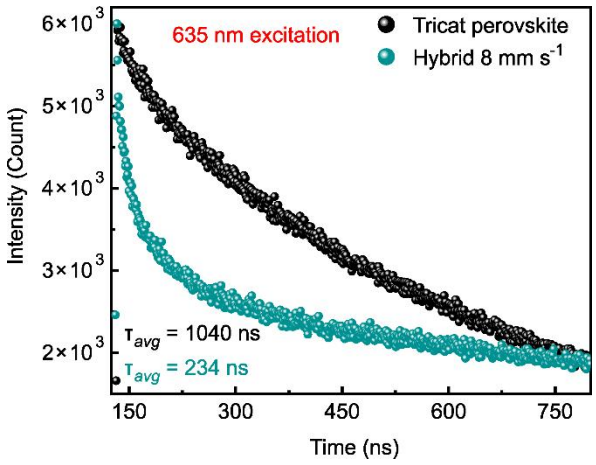

Fig. S11 Transient photoluminescence lifetime (TRPL) of control triple-cation and hybrid (4 mm s^{-1} – 10 mm s^{-1}) perovskites at 635 nm light excitation.

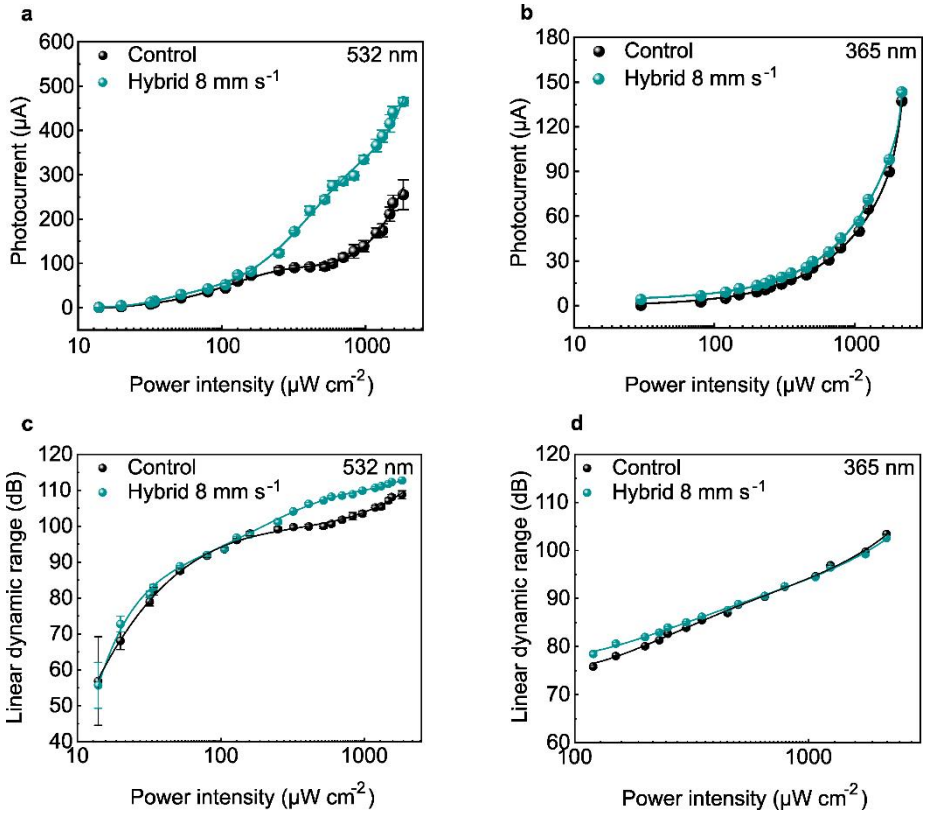

Fig. S12 a,b Photocurrent and **c,d** linear dynamic range (LDR) vs illumination power intensity comparison of control and hybrid 8 mm s^{-1} devices under 532 nm and 365 nm illumination.

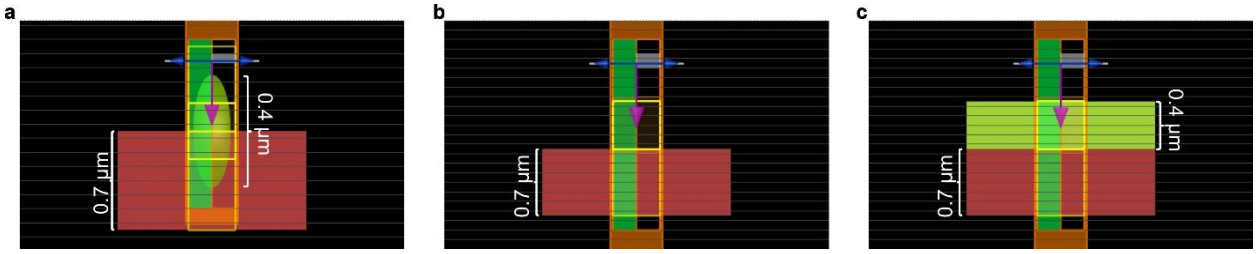

Fig. S13 Model information for **a** chocolate-chip-cookie perovskite, **b** control perovskite, and **c** perovskite/perovskite graded structures. The droplet size in the simulation was scaled down to reduce computational cost while preserving the same optical behavior.

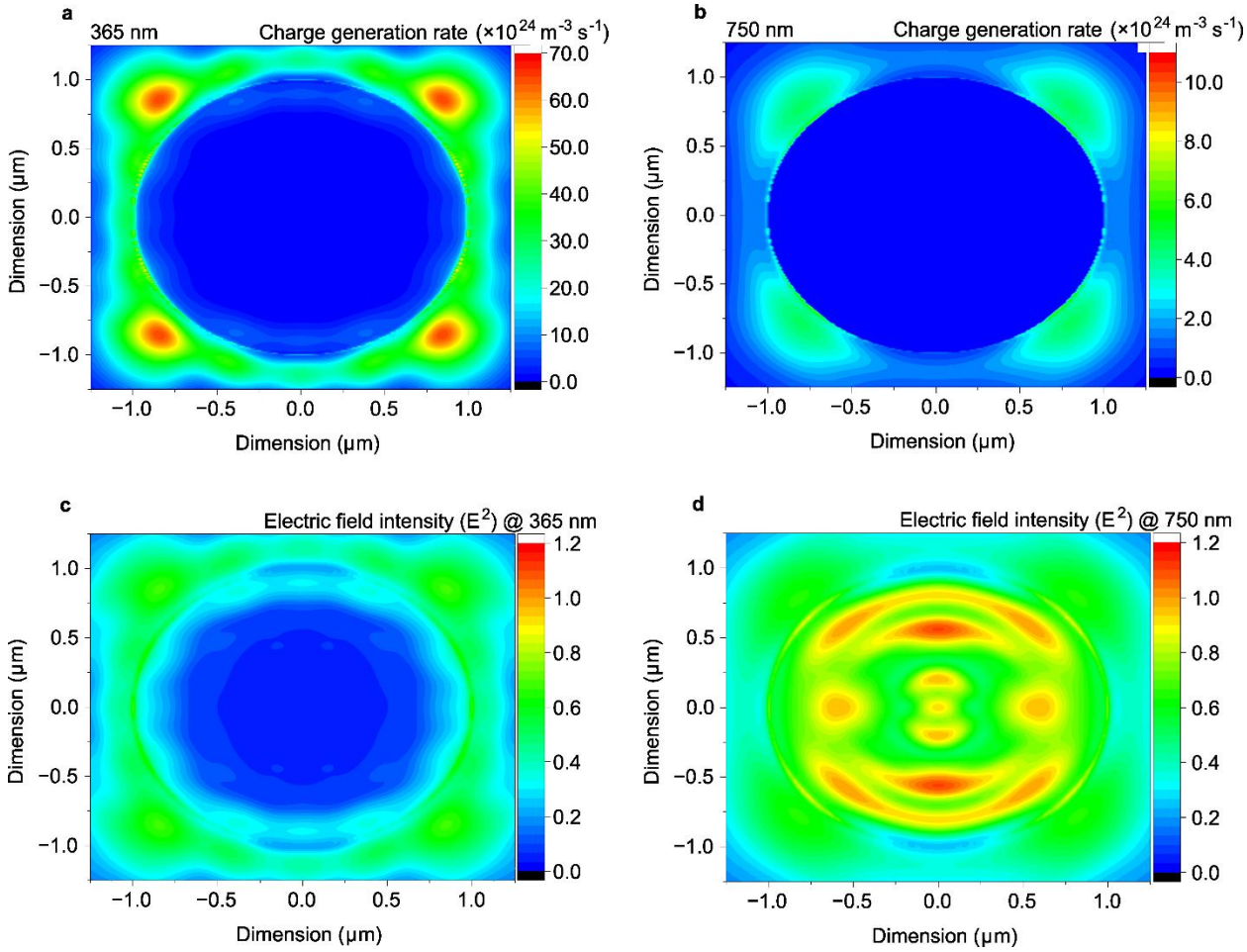

Fig. S14 Ansys Lumerical simulated **a, b** charge generation rate and **c, d** electric field intensity profiles of chocolate-chip-cookie perovskite under 365 nm and 750 nm light illuminations.

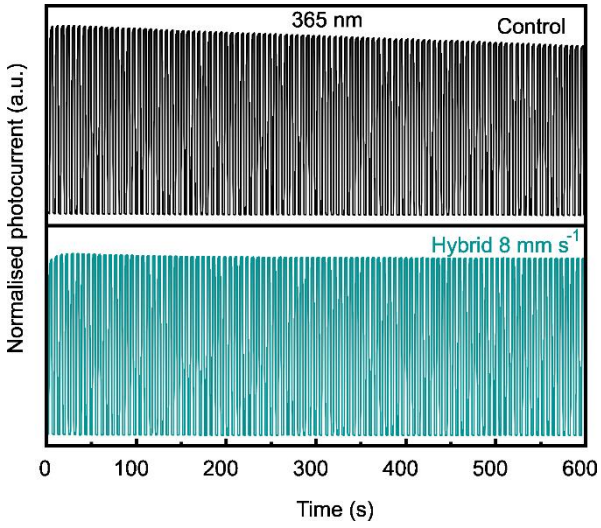

Fig. S15 Cyclic operational stability (100 cycles, 600 s) under periodically modulated illumination of 365 nm (UV).

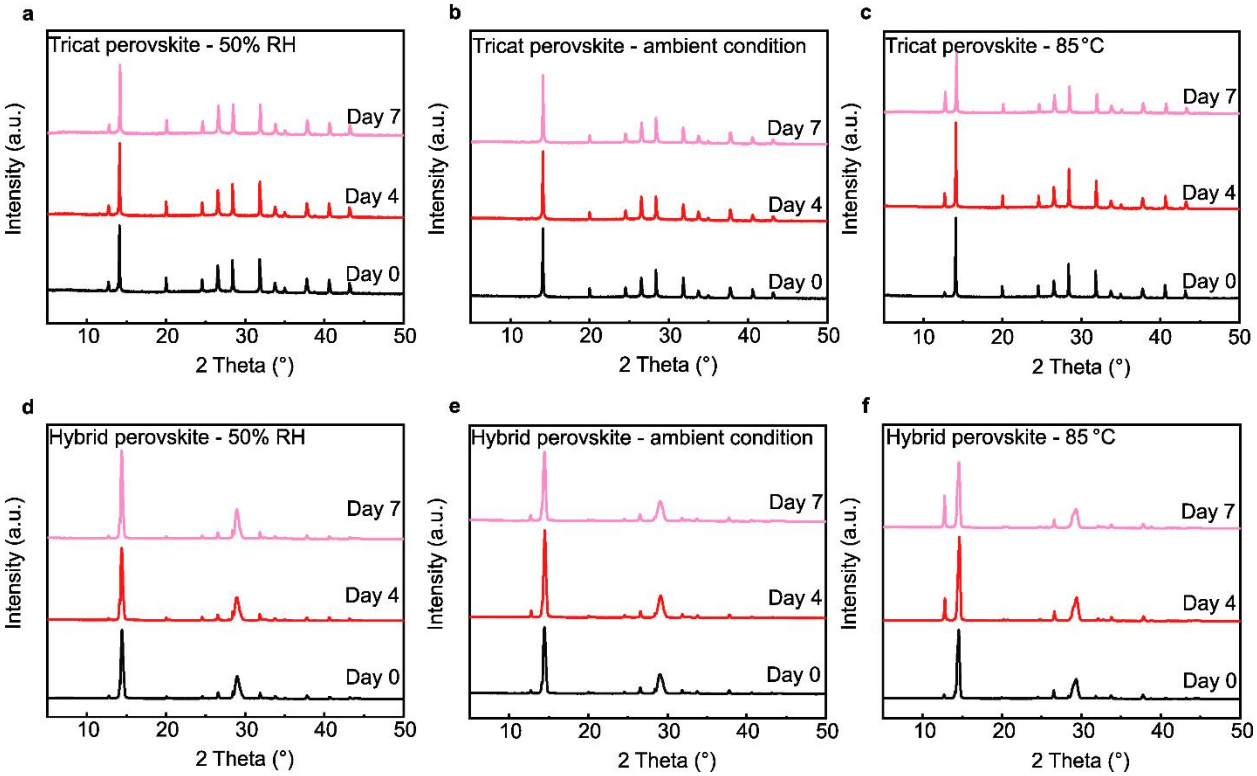

Fig. S16 a-c Triple-cation perovskite and **d-f** hybrid perovskite films' XRD stability data under 50% RH, ambient and 85 °C conditions.

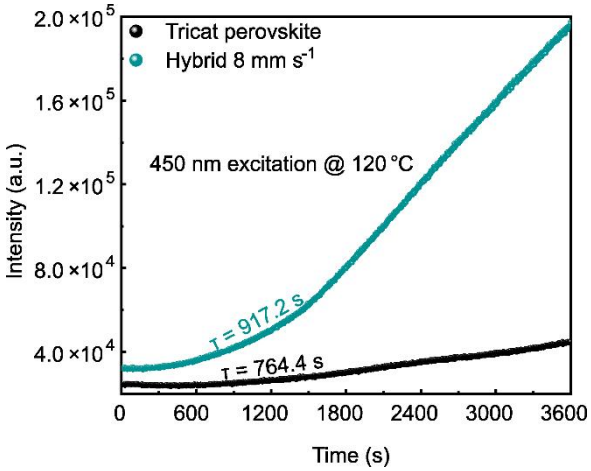

Fig. S17 The kinetic PL intensity trace of triple-cation and hybrid perovskites with the continuous excitation at 450 nm while locking down on the emission near 750 nm.

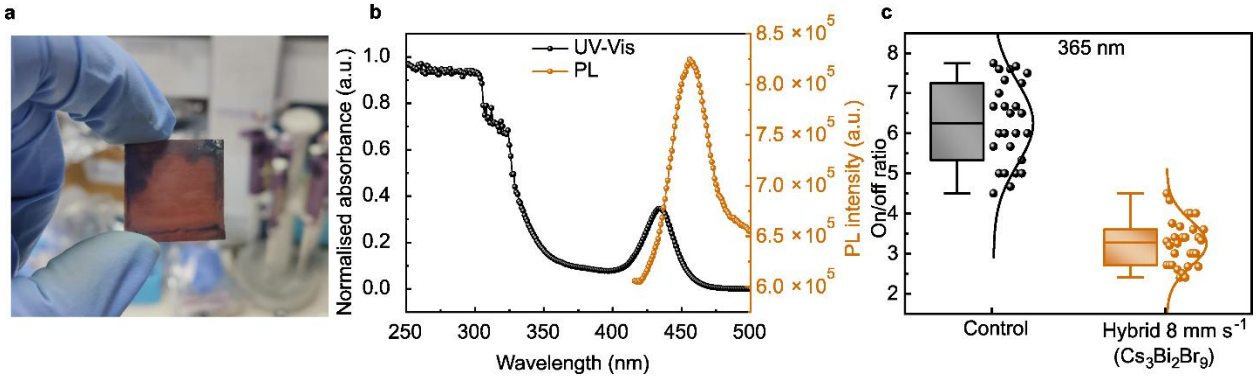

Fig. S18 a Photograph of $MAPbCl_3$ perovskite droplet embedded hybrid perovskite film. **b** UV-Vis and steady-state PL spectra of $Cs_3Bi_2Br_9$ perovskite. **c** Statistic on/off ratios of control and $Cs_3Bi_2Br_9$ perovskite droplet embedded hybrid perovskite devices under UVA 365 nm irradiation.

To further investigate the energy-selective photocurrent amplification in the UV region or the functional replacement for the second embedded perovskite, we explored the substitution of $CsPbBr_3$ with $MAPbCl_3$, a perovskite with a wider bandgap ($E_g \approx 2.96$ eV), suitable for enhanced UV light harvesting. However, a significant ion exchange reaction between Cl ions and the underlying perovskite results in phase instability and rapid degradation after fabrication, as evidenced in **Fig. S18a**. Consequently, we shifted our focus to all-inorganic perovskites as potential replacements. Furthermore, $Cs_3Bi_2Br_9$, a lead-free all-inorganic perovskite, was identified as a promising candidate, as it is widely used as a UV photodetector in previous studies, attributed to its wide bandgap ($E_g \approx 2.6$ eV).[10–12] Notably, its band energy levels ($E_{VB} = \sim$ -6.08 eV and $E_{CB} = \sim$ -2.78 eV) exhibit favorable alignment for integration into our hybrid perovskite structure. As shown in **Fig. S18b**, the absorption edge of $Cs_3Bi_2Br_9$ perovskite originated at ~470 nm, and the photoluminescence spectrum yielded a single sharp peak at ~468 nm, indicating its potential utility as a second embedded perovskite for UV detection sensors. Nevertheless, the $Cs_3Bi_2Br_9$ embedded hybrid perovskite sensor device demonstrated a weak

response to a 365 nm UV light source compared to that of the control device, as depicted in **Fig. S18c**.

REFERENCES

1. Zheng, E. et al. Solution-Processed Visible-Blind UV-A Photodetectors Based on $CH_3NH_3PbCl_3$ Perovskite Thin Films. *J Mater Chem C Mater* 2017, *5* (15), 3796–3806. doi: 10.1039/C7TC00639J.
2. Liu, S. et al. Polycrystalline Perovskite $CH_3NH_3PbCl_3$/Amorphous Ga_2O_3 Hybrid Structure for High-Speed, Low-Dark Current and Self-Powered UVA Photodetector. *J Alloys Compd* 2022, *890*, 161827. doi: 10.1016/j.jallcom.2021.161827.
3. Zhou, Y. et al. Halide-Exchanged Perovskite Photodetectors for Wearable Visible-Blind Ultraviolet Monitoring. *Nano Energy* 2022, *100*, 107516. doi: 10.1016/j.nanoen.2022.107516.
4. Nguyen, T. M. H. et al. Solution-Processed and Self-Powered Photodetector in Vertical Architecture Using Mixed-Halide Perovskite for Highly Sensitive UVC Detection. *J Mater Chem A Mater* 2021, *9* (2), 1269–1276. https://doi.org/10.1039/D0TA08738F.
5. Tong, G. et al. Enhancing Hybrid Perovskite Detectability in the Deep Ultraviolet Region with Down-Conversion Dual-Phase ($CsPbBr_3$ –Cs_4PbBr_6) Films. *J Phys Chem Lett* 2018, *9* (7), 1592–1599. doi: 10.1021/acs.jpclett.8b00429.
6. Xue, J. et al. Narrowband Perovskite Photodetector-Based Image Array for Potential Application in Artificial Vision. *Nano Lett* 2018, *18* (12), 7628–7634. doi: 10.1021/acs.nanolett.8b03209.
7. Wang, H. et al. 2D Perovskite Narrowband Photodetector Arrays. *J Mater Chem C Mater* 2021, *9* (34), 11085–11090. doi: 10.1039/D1TC03331J.
8. Wang, J. et al. Self-Driven Perovskite Dual-Band Photodetectors Enabled by a Charge Separation Reversion Mechanism. *Adv Opt Mater* 2021, *9* (17). doi: 10.1002/adom.202100517.
9. Shen, K. et al. Flexible and Self-Powered Photodetector Arrays Based on All-Inorganic $CsPbBr_3$ Quantum Dots. *Advanced Materials* 2020, *32* (22). doi: 10.1002/adma.202000004.
10. Liu, Y. et al. All-Inorganic Lead-Free NiO_x/$Cs_3Bi_2Br_9$ Perovskite Heterojunction Photodetectors for Ultraviolet Multispectral Imaging. *Nano Res* 2022, *15* (2), 1094–1101. doi: 10.1007/s12274-021-3608-4.
11. Zhou, X. et al. Wide-Bandgap All-Inorganic Lead-Free Perovskites for Ultraviolet Photodetectors. *Nano Energy* 2023, *117*, 108908. doi: 10.1016/j.nanoen.2023.108908.
12. Biswas, A. et al. Ag Intercalation in Layered Cs_3 Bi_2Br_9 Perovskite for Enhanced Light Emission with Bound Interlayer Excitons. *J Am Chem Soc* 2024, *146* (29), 19919–19928. doi: 10.1021/jacs.4c03191.